Feng *et al. Energy Mater* 2025;5:500002
DOI: 10.20517/energymater.2024.35

Energy Materials

Article

Open Access

Conjugated polyimides modified self-supported carbon electrodes for electrochemical conversion of CO_2 to CO

Daming Feng[1], Zuo Li[1], Huifang Guo[1], Xiaodong Sun[1], Peng Huang[1], Ying Sun[1], Hui Li[2], Tianyi Ma[2,*]

[1]Institute of Clean Energy Chemistry, Key Laboratory for Green Synthesis and Preparative Chemistry of Advanced Materials, College of Chemistry, Liaoning University, Shenyang 110036, Liaoning, China.
[2]School of Science, RMIT University, Melbourne, VIC 3000, Australia.

***Correspondence to:** Prof. Tianyi Ma, School of Science, RMIT University, 124 La Trobe Street, Melbourne, VIC 3000, Australia. E-mail: tianyi.ma@rmit.edu.au

How to cite this article: Feng D, Li Z, Guo H, Sun X, Huang P, Sun Y, Li H, Ma T. Conjugated polyimides modified self-supported carbon electrodes for electrochemical conversion of CO_2 to CO. *Energy Mater* 2025;5:500002. https://dx.doi.org/10.20517/energymater.2024.35

Received: 29 Apr 2024 **First Decision:** 13 Jun 2024 **Revised:** 3 Jul 2024 **Accepted:** 12 Jul 2024 **Published:** 18 Jul 2024

Academic Editor: Wei Tang **Copy Editor:** Fangling Lan **Production Editor:** Fangling Lan

Abstract

The electrochemical reduction of carbon dioxide (CO_2RR) offers a promising approach to address the dual challenges of energy scarcity and environmental degradation. This study presents a new, cost-effective, and scalable electrocatalyst: self-supporting carbon paper modified with porous conjugated polyimides. This innovative material facilitates efficient CO_2 conversion in aqueous media, eliminating the need for a pyrolysis step. The electrocatalyst's design utilizes a non-metallic organic polymer with a high density of nitrogen atoms, serving as active sites for catalysis. Its unique mesoporous microsphere structure comprises randomly stacked nanosheets that are generated *in situ* and aligned along the carbon fibers of carbon paper substrate. This architecture enhances both CO_2 adsorption and ensures proper electron transportation, facilitated by the conjugated structure of the polymer. Additionally, the inherent hydrophobicity of conjugated polyimides contributes to its robust catalytic performance in selectively reducing CO_2, yielding CO as the primary gaseous product with up to 88.7% Faradaic efficiency and 82.0 mmol g^{-1} h^{-1} yield rate. Therefore, the proposed electrocatalyst provides a sustainable solution for electrochemical CO_2RR catalyzed by non-metal organic materials, combining high efficiency with the advantages of a simple preparation process and the absence of costly materials or steps. This research contributes to the advancement of CO_2RR technologies, potentially leading to more environmentally friendly and energy-efficient solutions.

Keywords: Conjugated polyimides, self-supported electrodes, carbon dioxide reduction, carbon monoxide generation, electrocatalysis

INTRODUCTION

The escalating global challenge of carbon emissions is a pressing issue as the world endeavors sustainable solutions to mitigate the impacts of climate change[1]. The significant amounts of carbon dioxide (CO_2) emitted into the atmosphere from human activities pose both an environmental crisis and an underutilized resource[2]. Among the strategies to address this issue, converting CO_2 into valuable chemicals and fuels has emerged as a promising approach not only to reduce greenhouse gas emissions but also to establish a new carbon-neutral economy[3-5]. The electrochemical reduction of CO_2 (CO_2RR) is one of the most effective methods for this conversion, providing a direct and energy-efficient approach to transforming CO_2 into various value-added products, including carbon monoxide (CO), a crucial industrial feedstock[6,7]. The electrochemical CO_2RR holds the potential to offer a dual solution: mitigating carbon emissions by converting excess CO_2 into valuable products and storing energy from renewable sources, such as solar and wind, in chemical bonds[8,9]. However, the full potential of this technology can only be realized through significant improvements in selectivity towards specific products, particularly CO. This is because CO serves as a valuable precursor in the synthesis of various chemicals and can act as a building block for the production of synthetic molecules, establishing a direct connection between renewable energy sources and the chemical industry[10-12].

The pursuit of efficient CO_2 electroreduction hinges on the selection of appropriate electrocatalysts. Among these, precious metals have long been esteemed for their exceptional selectivity and reactivity[13,14]. However, their widespread utilization is hampered by their prohibitive costs and susceptibility to poisoning. This limitation has prompted researchers to explore alternative options, with non-precious metals emerging as more economically viable alternatives. In this regard, transition metal-based nano materials[15-17] and main group metals[18,19] have drawn widespread attention for CO_2RR. Among them, the first-row transition metal-containing and easily available systems toward CO_2-to-CO conversion are very promising for the industrial application due to their low cost and high activity[20-22]. Additionally, the emergence of metal-free carbonaceous materials, such as porous carbon, graphene, carbon nanotubes, and carbon quantum dots, also offers a promising avenue for CO_2 electroreduction[23-26]. These materials boast both cost-effectiveness and durability, representing a compelling alternative to traditional metal catalysts. Among these, the nitrogen-doped carbon materials presented their robust and effective catalytic performance for the generation of syngas with various ratios[27]. Additionally, other non-metal atom-doped carbons, such as sulfur[28], phosphorous[29], boron[30], and selenium[31,32], also exhibited considerable ability in electrochemical conversion of CO_2. However, challenges remain, particularly in ensuring consistent active site distribution, a concern stemming from the pyrolysis process used in their synthesis.

Conjugated polyimides (CPIs) represent a novel class of electrocatalysts distinguished by their tunable electronic properties, which can be precisely modified through chemical alterations[33-35]. They also exhibit inherent stability, surpassing many traditional electrocatalysts[36,37]. These polymers demonstrate remarkable flexibility in morphological control at the nanoscale, thereby enhancing surface area and porosity to facilitate abundant active sites and enhance mass transport[38,39]. Their intrinsic redox activity and mechanical strength support efficient electron transfer and eliminate the need for binders or substrates, respectively. Additionally, CPIs offer a cost-effective alternative to metal catalysts. They can be synthesized to target specific applications, rendering them compatible with various electrolytes for a broad range of electrochemical devices[34,35]. These attributes position CPIs as a promising material for the selective and sustainable conversion of CO_2 to CO. Han *et al.* developed a series of 2D covalent organic frameworks with cobalt(II)-phthalocyanine sites (CoPc-PI-COFs) as electrocatalysts for efficient CO_2RR, yielding CO

products with up to 97% Faradaic efficiency (FE) at -0.8 V *vs.* RHE (Reversible Hydrogen Electrode) with 21.1 mA partial current density[40]. Subsequently, they further developed several 3D CoPc-PI-COFs for electrocatalytic conversion of CO_2 to CO[41]. The 3D porous structure increased the exposure of active electrocatalytic sites, resulting in enhanced current density for the production of CO with up to 96% FE at -0.9 V *vs.* RHE. The current landscape of polyimide electrocatalysts for CO_2 reduction is predominantly characterized by the incorporation of M-N_4 sites, typically derived from metal phthalocyanine or metalloporphyrin precursors. Despite these advances, the extensive application of truly metal-free polyimides as electrocatalysts in CO_2 reduction reactions has not been widely reported, representing an opportunity for further investigation and development.

With our continuous interest in electrocatalysis[42,43]. Herein, a metal-free self-supported carbon paper (CP)-based CPI organic heterogeneous catalyst, denoted as CPI/CP, was developed for effective electrochemical CO_2RR. Compared to CPI powders, the *in situ* polymerized CPI on the fibers of CP exhibited microspheres without active exceeded amino groups. Characterization and electrochemical studies showed that the microspherical morphology and thin-layered CPI nanosheets provided broadened conjugated structure and intrinsic hydrophobicity for facilitating the electron transfer and suppressing the hydrogen evolution reaction (HER) process at the same time. The triazine ring and imide group were demonstrated as the active sites for the adsorption and activation of CO_2, promoting the efficiency and selectivity for the CO production.

EXPERIMENTAL

Synthesis of conjugated polyimide (CPI) powder

The CPI powder was synthesized following the literature procedure[44] with slight modification, and denoted as CPI-A. First, 1,2,4,5-Benzenetetracarboxylic anhydride (PMDA, 981.5 mg, 4.5 mmol) and H_2O (162 μL) were added into 1-methayl-2-pyrrolidinone (NMP, 20 mL) in an autoclave. Then, melamine (MA, 378.4 mg, 3 mmol) dispersed in a 20 mL solution of NMP was dropwise added into the mixture under stirring for 1 h at 25 °C. After reacting at 210 °C for 24 h in the sealed autoclave, the mixture stayed still for another 24 h. After washing with NMP, *N*,*N*-dimethyl formamide (DMF), hot water, and ethanol to remove any impurities, the yielding dark brown solids were dried at 100 °C for 12 h in a vacuum oven. The obtained products were directly used without any further purification for characterization and subsequent experiments.

Synthesis of self-supported CPI/CP

The CPI/CP was fabricated following a procedure similar to the synthesis of CPI-A. At first, the CP (1 cm × 2 cm) was rinsed in concentrated HCl (12 M) solution for 10 min to remove surface impurities and enhance the hydrophilicity, which benefits the *in-situ* growth of CPI. After washing with deionized water, the CP was dried at 60 °C for 8 h in a vacuum oven. PMDA (981.5 mg, 4.5 mmol) and H_2O (162 μL) were first added into 20 mL NMP in an autoclave. Then, MA (378.4 mg, 3 mmol) dispersed in a 20 mL solution of NMP was dropwise added into the mixture under stirring for 1 h at 25 °C. Subsequently, a piece of pre-treated CP (1 cm × 1.5 cm) was placed in the autoclave. After reacting at 210 °C for 24 h in the sealed autoclave, the mixture stayed still for another 24 h. After washing with deionized water to get rid of the solvents, the CPI-coated CP was air-dried in the fume hood overnight. The resulting CPI/CP was directly used without any further purification.

Synthesis of CPI powder in sealed tubes

The CPI powder synthesis was performed in a vacuum-sealed Pyrex tube, denoted as CPI-S. Initially, 981.5 mg (4.5 mmol) of PMDA and 378.4 mg (3 mmol) of MA were dissolved in a 20 mL NMP solution within a 100 mL Pyrex tube. The tube was subsequently frozen using liquid nitrogen, evacuated, and flame-

sealed. The reaction was then conducted at 120 °C for 120 h. The resulting solids were sequentially washed with NMP, DMF, hot water, and ethanol to remove impurities. The dark brown solid product was then dried at 100 °C for 12 h in a vacuum oven. The resulting CPI-S powder was directly used for characterization and subsequent experiments without further purification steps.

The additional detailed experimental data, such as reagents, characterizations, and electrochemical measurements, are provided in the Supplementary Materials.

RESULTS AND DISCUSSION

Synthesis and characterization of catalysts

Scheme 1 illustrates the systematic procedure for preparing self-supported CPIs on CP substrate (CPI/CP). The CPI/CP composite was synthesized via solvothermal synthesis of CPI with PMDA and MA at 210 °C with pre-treated CPs additionally placed in the autoclave. Upon visual inspection of the fabricated CPI-CP, the surface color transitioned from dark grey to a bit yellowish, indicating the successful CPI growth on the CP surface. For a comprehensive investigation of CPI materials, CPI powders were also prepared via solvothermal condition in an autoclave (CPI-A) and a vacuumed sealed tube (CPI-S) without any heterogeneous substrate. Subsequently, the CPI-A and CPI-S powders were introduced onto the CP with the aid of Nafion solutions. All the three fabricated working electrodes were directly used in the following electrolysis after activation without any other operations.

The surface morphologies of these materials were investigated using scanning electron microscopy (SEM), atomic force microscopy (AFM), and transmission electron microscopy (TEM). SEM images clearly depicted the formation of CPI microspheres with diameters ranging from 2-10 μm, adhering to the fibers of CP [Figure 1A]. Additionally, as illustrated in Figure 1B, regular microspheres were constructed from CPI nanosheets, exhibiting solid structures with irregular stacking. Transverse surface and partially enlarged images are presented as Figure 1C and D, revealing CPI nanosheets stacked randomly with rough boundaries. SEM images labeled CPI-A and CPI-S are presented Figure 1E and F, respectively. A mixture of microspheres and microsheets is observed in the CPI-A sample, indicating shape transformation during the solvothermal process. Conversely, microsheets with smooth boundaries were the predominant morphology observed in the CPI-S sample. Moreover, TEM images of CPI dispersed ultrasonically in CPI-A [Figure 1G] and exfoliated from CPI/CP [Figure 1H] reveal the 2D nanoscale structure of CPI sheets, potentially enhancing electrical conductivity[45]. AFM images also revealed the micrometer-scale dimensions of CP microspheres [Figure 1I and J]. As shown in Figure 1K, energy dispersive X-ray spectroscopy (EDS) mapping images confirmed the even distribution of each element, indicating the construction of CPI through covalent bonding of organic substrates.

To obtain more detailed information on the structure and composition of CPI materials, additional characterization techniques were employed. In the Fourier transform infrared spectroscopy (FT-IR) spectrum comparison, the characteristic peaks around 1,362, 1,785, and 3,400 cm^{-1} corresponded to the stretching vibrations of C-N-C, C=O, and N-H bonds, respectively [Figure 2A][46]. Noticeable N-H stretching bands were observed in the spectra of CPI-A and CPI-S, suggesting the presence of MA or its oligomers in these structures. Furthermore, the ultraviolet-visible (UV-Vis) diffuse reflectance spectra (DRS) showed that CPI-A and CPI-S shared similar absorption peaks with PMDA, albeit with a slight red shift, whereas CPI/CP exhibited a broad absorption spectrum [Figure 2B]. This confirmed the enhanced conjugated structure of CPI/CP, potentially facilitating rapid electron transport. Moreover, the X-ray diffraction (XRD) patterns of these materials revealed a more ordered structure for CPI/CP, characterized by fewer peaks between 10°-35° compared to CPI-A and CPI-S [Supplementary Figure 1][47]. Additionally,

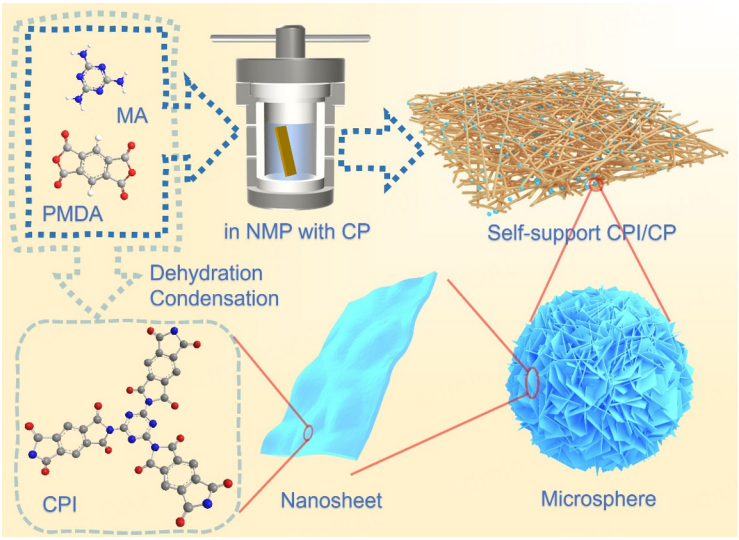

Scheme 1. The synthetic diagram of *in-situ* growth of CPI nanosheets on CP thermodynamically.

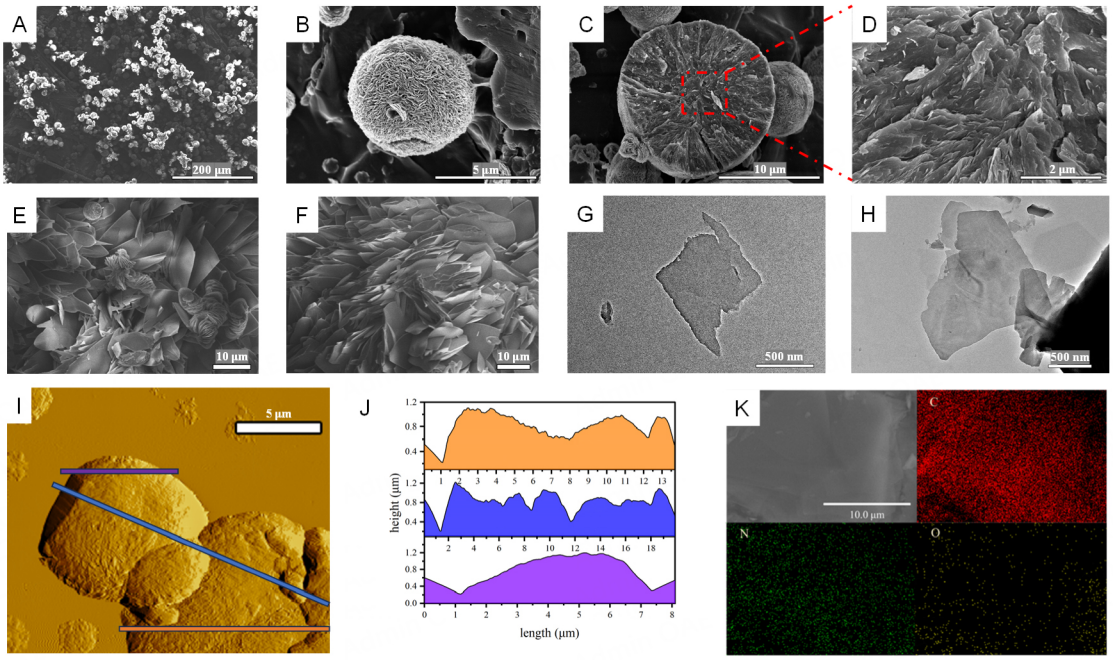

Figure 1. SEM images of (A-D) CPI/CP, (E) CPI-A, and (F) CPI-S. TEM images of (G) CPI-A and (H) CPI/CP. (I) AFM measurements of CPI/CP. (J) Corresponding height curves for the selective areas in (I). (K) EDS mapping image of CPI/CP.

the peaks at 167.29, 157.02, 137.34, and 120.08 ppm in the cross-polarization magic angle spinning nuclear magnetic resonance (CP MAS NMR) spectrum can be attributed to hydrogen bonded benzylic, imide bonded benzylic, carbonyl, and triazine carbons in the CPI structure [Figure 2C]. Meanwhile, the X-ray photoelectron spectroscopy (XPS) demonstrated the absence of metal elements within the CPI material, consistent with the findings of EDS mapping[46]. In the full spectrum, the peaks centered at 286.6, 399.4, and 531.0 eV were attributed to C 1s, N 1s, and O 1s, respectively [Figure 2D]. In the C 1s spectrum, the 284.8 eV represents graphite carbon, inferring the conjugated structure of CPI [Figure 2E]. Additionally, the 286.3 and 288.4 eV were mainly attributed to the generated imide and intrinsic triazine groups in the CPI.

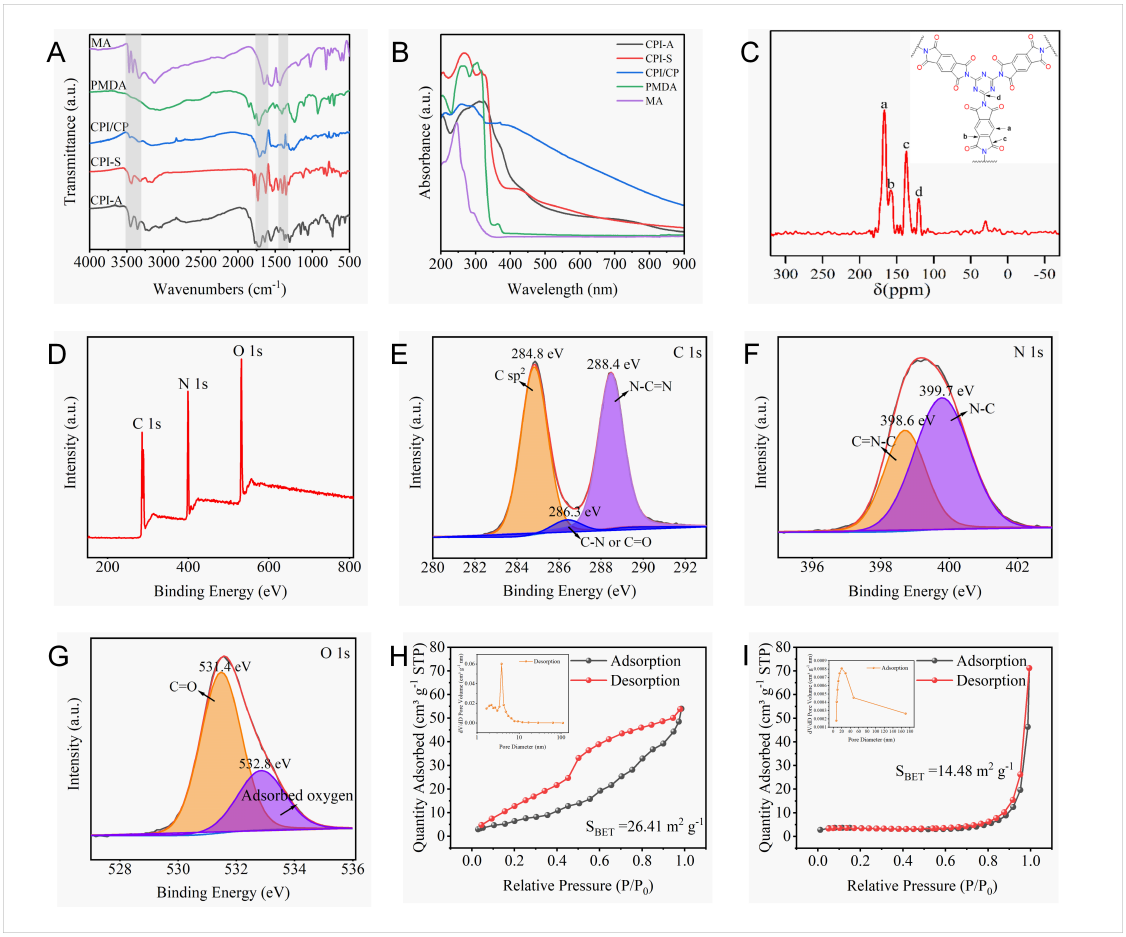

Figure 2. (A) FT-IR and (B) solid-state UV-Vis DRS spectra of CPI/CP, CPI-A, CPI-S and raw materials. (C) CP MAS NMR spectrum of CPI exfoliated from CPI/CP. (D) XPS spectra of CPI/CP. (E) C 1s, (F) N 1s, and (G) O 1s XPS spectra of CPI/CP. N_2 adsorption-desorption isotherms and pore size distribution of (H) CPI-S and (I) CPI/CP.

In N 1s spectrum, the peaks at 398.6 and 399.7 eV can be denoted as the triazine N and imide N, respectively, further certifying the successful synthesis of CPI in a bonding manner [Figure 2F]. While in the O 1s spectrum, apart from the peak at 531.4 eV for carbonyl O in the imide group, there was also a peak at 532.8 eV representing the adsorbed O [Figure 2G]. The signals in XPS collectively provide compelling evidence for the formation of CPI from PMDA and MA. Furthermore, thermogravimetric analysis (TGA) and corresponding derivative thermogravimetry (DTG) of CPI/CP revealed that the majority of CPI decomposed at 395 °C, confirming its relatively higher stability owing to the conjugated structure [Supplementary Figure 2][46,47]. To elucidate the specific surface areas and pore size distributions of CPI materials, N_2 adsorption-desorption tests were carried out for CPI-S and CPI/CP. A reversible type IV isotherm with an H4 hysteresis loop was presented by CPI-S, suggesting its mesoporous nature with a layered structure [Figure 2H]. The surface area of CPI-S was calculated to be 26.41 m^2/g using the Brunauer-Emmett-Teller (BET) model and the pore size distribution was calculated using the Barrett-Joyner-Hallender method, of which the peak value was 3.84 nm. These mesoporous structures are generated by the regular arrangement of CPI layers. In contrast, CPI/CP exhibits a type IV isotherm with an H1 hysteresis loop, indicative of a spherical cluster morphology with a calculated surface area of 14.48 m^2/g [Figure 2I]. The moderated surface area results from the random arrangement of CPI layers, forming microspheres that provide a reduced contact surface area, enhancing selectivity in production. The pore size distribution presented a wide range of 10-25 nm as mesoporous.

Electrochemical CO_2RR performance

Electrolysis was performed in a H-cell equipped with three electrodes: the fabricated working electrode, a Pt foil counter electrode, and an Ag/AgCl reference electrode. The catalytic activities of CO_2RR were initially assessed by comparing linear sweep voltammetry (LSV) measurements in an Ar/CO_2 saturated 0.5 $KHCO_3$ electrolyte. The on-site potential of CPI/CP in a CO_2 atmosphere is lower than that in an Ar atmosphere, resulting in a clear reductive potential window between -0.4 and -1.1 eV [Figure 3A]. While the CPI-A and CPI-S provide higher current density in Ar than in CO_2, which may be due to the inactive catalytic performance for the conversion of CO_2 molecules and the prohibition effect of HER from adhesive CO_2 [Supplementary Figure 3]. Compared to CPI-A and CPI-S, CPI/CP exhibited significant suppression of HER and a remarkable enhancement of CO_2RR despite a slight decrease in current density. Subsequently, potentiostatic tests of CO_2RR were conducted at five potentials (-0.50, -0.55, -0.60, -0.65, and -0.70 V *vs.* RHE) over a 1-h period at each potential with constant CO_2 gas input [Supplementary Figure 4]. With potentials lower than -0.6 V *vs.* RHE, the current densities of electrolysis catalyzed by CPI/CP were generally lower than those of CPI-A and CPI-S. Notably, at -0.65 V *vs.* RHE, where the highest catalytic activities exhibited, the CPI/CP presented average current density at 2.8 mA cm^{-2}, while at 3.2 mA cm^{-2} for those catalyzed by CPI-A and CPI-S. The output gases and electrolyte liquids were collected for further determination of products. Aside from CO and H_2 detected by specific gas chromatography equipped with Flame Ionization Detector (FID) and Thermal Conductivity Detector (TCD), no other obvious signals indicating the generation of alternative carbon products were observed in any of the collected samples [Supplementary Figure 5]. Furthermore, no liquid products were detected by the ^{1}H nuclear magnetic resonance (NMR) of the electrolytes using the Water Eliminated Fourier Transform (WEFT) technique [Supplementary Figure 6]. At each potential, the electrolysis was conducted three times independently under identical conditions, and the corresponding FEs and yield rates mentioned below refer to the average values of the calculated results. Throughout all the potentiostatic tests, CPI/CP consistently exhibited exceptional catalytic performance compared to the others at each examined potential. As depicted in Figure 3B, at -0.5 V *vs.* RHE, CPI/CP demonstrated the highest FE_{CO} of 54.0%, while CPI-A exhibited a moderated FE_{CO} at 19.6% and CPI-S showed a negligible result. As the potential shifted to the negative, the FE_{CO} reached a maximum of 88.6% at -0.65 V *vs.* RHE under the catalysis of CPI/CP, followed by a decrease. Meanwhile, the FE_{CO} values of CPI-A and CPI-S followed a similar trend, reaching their highest values at -0.65 V *vs.* RHE, with 59.2% and 29.6%, respectively. As shown in Figure 3C, the CO yield rate of CPI/CP reached 82.0 mmol g^{-1} h^{-1} at -0.65 V *vs.* RHE, which is 1.76 and 3.63 times higher than those of CPI-A and CPI-S. In contrast to the trend in FE_{CO}, the CO yield rates decreased dramatically at lower overpotentials, such as -0.55 and -0.50 V *vs.* RHE. This phenomenon indicates that the differences between the partial currents of CO and H_2 are relatively lower at low overpotentials than those of higher ones, in consistency with potential window discovered in LSV spectrum. Based on the characterization of CPI materials, the robust electrocatalytic activity and production selectivity of CPI/CP can be attributed to their extensive conjugative property and random stacking of CPI nanosheets, which balance electron transfer throughout the organic conjugated structure and CO_2 adsorption on the imide/triazine nitrogen containing sites[48]. Despite the regularly arranged CPI nanosheets in CPI-S possessing a layer-by-layer nanostructure and an enlarged surface area with concentrated pore size distribution, the dominant HER process in the aqueous solution still significantly influences the CO_2RR.

Subsequent experiments were conducted using various counter electrodes to demonstrate the active role of Pt in the electrochemical CO_2RR process[49]. As depicted in Figure 3D, neither the blank CP nor the graphite counter electrodes provided significant enhancement for CO production, likely due to their inherent inertness to the oxygen evolution reaction, which offers minimal promotion of the reduction overpotential [Supplementary Figure 7]. Furthermore, the influence of electrolyte pH on the reaction was examined in controlled tests [Supplementary Figure 8]. With equal molar of potassium ions, K_2SO_4 (0.25 M, pH = 7) and

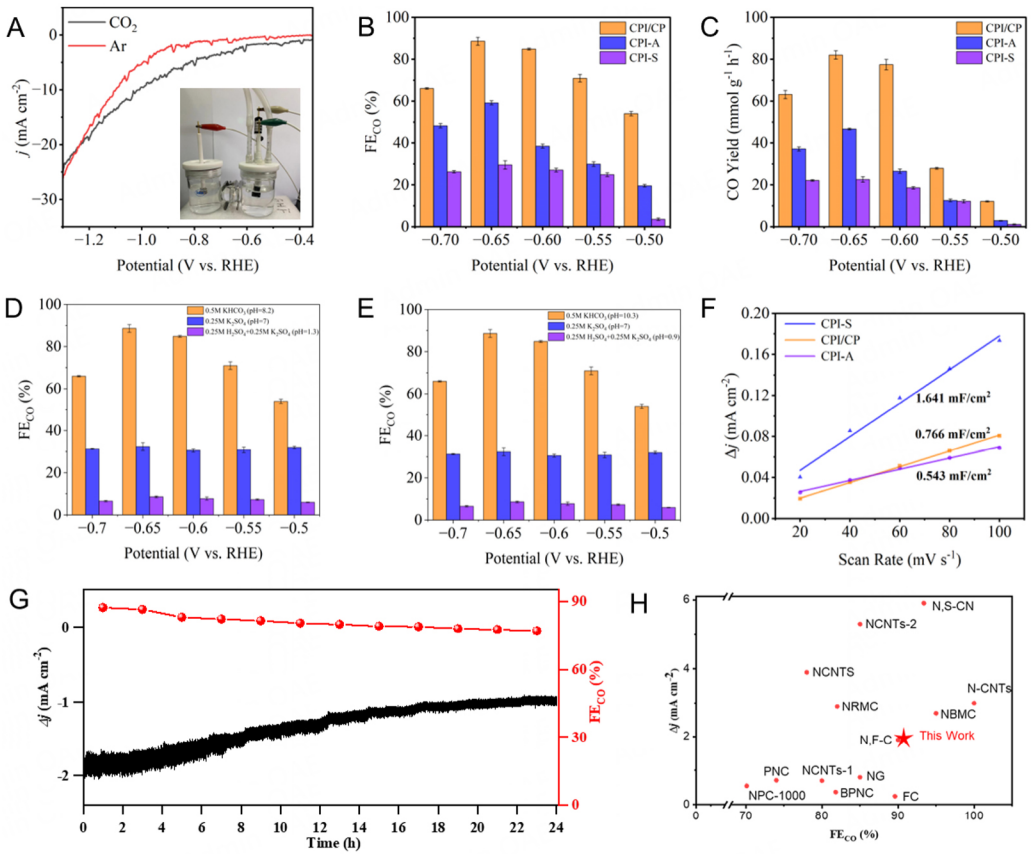

Figure 3. Electrochemical CO_2RR performance of CPI/CP, CPI-A, CPI-S. (A) LSV curves in a CO_2-saturated 0.5 M $KHCO_3$ electrolyte. (B) FE_{CO}. (C) CO yield rates. (D) FE_{CO} with various counter electrodes. (E) FE_{CO} with various electrolysis media. (F) C_{dl}. (G) Stability test of CPI/CP at -0.65 V *vs.* RHE for 24 h. (H) FE_{CO} comparison of non-metal electrocatalysts.

$KHSO_4$ (0.5 M, pH = 1.3) were selected as neutral and acidic electrolytes, respectively, because the alkaline conditions were neutralized by the CO_2 that was bubbled through the electrolyte. The FE and CO yield rate after 1 h of electrolysis are presented in Figure 3E. It is evident that the mild alkalinity of $KHCO_3$ (0.5 M, pH = 8.2) is conducive to the reaction, whereas the increased hydrogen evolution in neutral and acidic electrolytes impedes the electrochemical conversion of CO_2, leading to reduced CO production. Besides, the pH value of $KHCO_3$ electrolyte remained the same after prolonged electrolysis, indicating the carbon source of product CO is the inlet CO_2 gas. Moreover, the electrochemical surface area (ECSA) of CPI electrocatalysts was determined by measuring the double-layer capacitance (C_{dl}) in the non-Faraday reaction region of the cyclic voltammetry (CV) curve at various scan rates, reflecting the quantity of active surface sites [Supplementary Figure 9]. After the data collection and linear correlation, the C_{dl} values for the CPI-S, CPI-A, and CPI/CP are 1.641, 0.543, and 0.766 mF cm^{-2}, respectively [Figure 3F]. Originating from the solvothermal method using autoclaves, CPI-A and CPI/CP exhibited C_{dl} values with minor difference under electrolytic circumstances. CPI-S obtained the highest C_{dl} value, indicating its excellent electron transportation ability. However, despite the higher C_{dl} value, larger ECSA, and more exposed active sites of CPI-S, these characteristics did not confer any advantages in selective electrocatalytic CO_2RR, as the inevitable HER process was improved with these conditions in aqueous electrolysis. Moreover, the CPI/CP electrocatalyst exhibited considerable durability and stability during the electrolysis at -0.65 V *vs.* RHE for continuous 24 h [Figure 3G]. Although the current density has dropped by approximately 40%, the FE_{CO} has not decreased much, from 93.1% to 78.3%. The surface morphology of CPI/CP was also examined after

long-term electrocatalysis for CO_2RR. The enhanced electrocatalytic performance of CPI/CP compared to those of carbon material-based catalysts can be concluded in Figure 3H and Supplementary Table 1. Considering its low cost and pyrolysis-free synthetic route, this stable and active electrocatalyst has a good application prospect in the conversion of CO_2. The electrochemical assessments of CPI electrocatalysts elucidate their role in CO_2RR. While CPI-S exhibits superior electron transport, it does not confer selectivity advantages, highlighting the dominance of the HER process. Conversely, CPI/CP demonstrates durability and stability during prolonged electrolysis, indicating their potential for sustainable electrochemical CO_2 conversion.

To further assess the stability of polymer catalysts, we characterized catalysts after extended electrolysis and compared them with unexposed catalysts. The SEM image shows that the microspheres on the CP electrode surface almost disappeared compared to the fresh fabricated and activated ones [Figure 4A]. Furthermore, contact angle measurements of water droplets on CPI/CP before and after long-term electrolysis in aqueous solution were conducted, yielding values of 122.1° and 79.0°, respectively, indicating a change in hydrophobicity during the electrocatalytic process [Figure 4B]. Despite some catalyst detachment during the process, the TEM image of CPI nanosheets was still observable post-reaction, suggesting that the structural integrity of the catalyst was largely maintained [Supplementary Figure 10]. Additionally, the charge transfer resistance (R_{ct}) of CPI/CP was examined using electrochemical impedance spectroscopy (EIS) [Figure 4C]. Nyquist plots indicate that CPI/CP is controlled by both charge transfer and substance diffusion during electrochemical CO_2RR processes, where electrochemical polarization coexists with concentration polarization. After the electrolysis, the R_{ct} of CPI/CP reduced from 11.12 to 2.76, inferring swift electron transport on the catalyst compared to that before electrolysis. The increased slope (from 2.88 to 3.11) at the low frequency zone indicates the faster mass transport for the catalyst after the electrolysis. Considering the catalytic performance and the characterization of the CPI/CP before and after electrolysis, such a transformation of the catalyst occurring can be ascribed to the disappearance of the mesosphere morphology. Such rearrangement of the catalyst surface facilitates the electron transfer, mass transport, and hydrophilicity of the surface, which attenuates the selectivity for CO_2 conversion by emerging HER.

Theoretical calculations

Density Functional Theory (DFT) calculations were employed to gain insights into the catalytic mechanism of CPI structure. The free energy diagrams for the CO_2RR demonstrate that CO_2 molecules are easily adsorbed onto the catalyst surface, a process that is enhanced by the activated CPI structure [Figure 4D]. The activation of adsorbed CO_2 to form *COOH is identified as the potential rate-determining step on CPI, with a relatively low energy barrier that implies fast reaction dynamics for CPI unit. Furthermore, the lower energy required to generate the intermediate *CO and the final product CO underscores the thermodynamic favorability of CO_2RR on CPI structure. The DFT analysis also suggests that the active sites on CPI play a crucial role in lowering the activation energy for CO_2 conversion, thereby facilitating the CO_2RR process. This enhanced activation capability, coupled with the thermodynamic advantage, indicates that CPI/CP can efficiently catalyze the conversion of CO_2 to CO, leading to improved CO_2RR performance. The results from DFT calculations thus provide a molecular-level understanding of the catalyst's activity and its ability to promote the *in-situ* generation of CO, which is crucial for the development of more efficient CO_2RR catalysts.

CONCLUSIONS

In summary, a self-supported composite of CPI/CP was synthesized via a straightforward, pyrolysis-free process, which effectively and selectively facilitated the electrochemical reduction of CO_2 to CO. After thorough comparison and extensive characterization of various synthetic methods, it was found that CPI-S

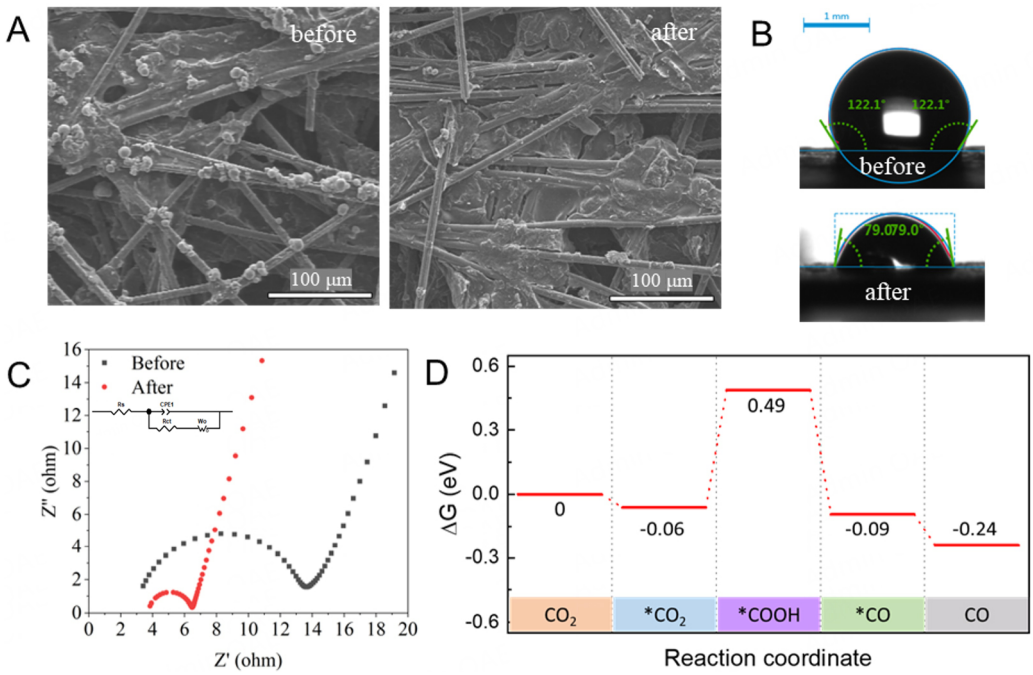

Figure 4. (A) SEM images of CPI/CP and (B) contact angle of water droplet on CPI/CP before (up) and after (down) long-term electrolysis. (C) Nyquist plots for CPI/CP before and after electrolysis. (D) Free energy diagram of CPI unit for CO_2RR.

exhibited a more regular structure, characterized by a 2D nanosheet morphology with layers that aggregate in a layer-by-layer fashion, and a larger surface area. In contrast, CPI/CP, which featured a microspherical morphology with randomly stacked CPI nanosheets, significantly outperformed CPI-A and CPI-S in terms of activity and selectivity for CO_2RR. This was evidenced by a maximum FE_{CO} of 88.6 % and a CO yield rate reached 82.0 mmol g^{-1} h^{-1} at an applied potential of -0.65 V *vs.* RHE. Despite a reduction in surface area and moderate ECSA compared to CPI-S, the enhanced conjugated properties of CPI/CP specifically preserved the electron transfer capability. Additionally, the sufficient hydrophobicity of the material effectively mitigated the HER process. This study presents a novel strategy for the design of cost-efficient and eco-friendly benign non-metal electrocatalysts, aimed at the efficient production of CO via the electrochemical CO_2RR.

DECLARATIONS

Acknowledgments

The authors thank Shiyanjia Lab (www.shiyanjia.com) for support of the BET, XPS, and CP MAS NMR tests.

Authors' contributions

Conceived the research and designed the experiments: Feng D, Huang P
Prepared the conjugated polyimides and catalysts, carried out the electrochemical testing: Li Z, Guo H
Completed the manuscript: Feng D, Sun X, Li Z
Discussed and revised the manuscript: Feng D, Sun X, Sun Y, Li H, Ma T

Availability of data and materials

The details of materials and reagents, instrumentation and characterizations, and electrochemical measurements were shown in the Supplementary Materials.

Financial support and sponsorship

This work was supported by the National Natural Science Foundation of China (Nos. 52071171, 52202248), Key Research Project of the Department of Education of Liaoning Province (LJKZZ20220015), Australian Research Council (ARC) through Future Fellowship (FT210100298), Discovery Project (DP220100603) and Linkage Project (LP210200504, LP220100088) schemes, the Australian Government through the Cooperative Research Centres Projects (CRCPXIII000077), the Australian Renewable Energy Agency (ARENA) as part of ARENA's Transformative Research Accelerating Commercialisation Program (TM021), and Natural Science Foundation of Liaoning Province (general program) (2020-MS-137).

Conflicts of interest

All authors declared that there are no conflicts of interest.

Ethical approval and consent to participate

Not applicable.

Consent for publication

Not applicable.

REFERENCES

1. Seddon N. Harnessing the potential of nature-based solutions for mitigating and adapting to climate change. *Science* 2022;376:1410-6. DOI PubMed
2. Wang W, Zeng C, Tsubaki N. Recent advancements and perspectives of the CO_2 hydrogenation reaction. *Green Carbon* 2023;1:133-45. DOI
3. Hepburn C, Adlen E, Beddington J, et al. The technological and economic prospects for CO_2 utilization and removal. *Nature* 2019;575:87-97. DOI
4. Kamkeng ADN, Wang M, Hu J, Du W, Qian F. Transformation technologies for CO_2 utilisation: current status, challenges and future prospects. *Chem Eng J* 2021;409:128138. DOI
5. Mao J, Wang Y, Zhang B, et al. Advances in electrocarboxylation reactions with CO_2. *Green Carbon* 2024;2:45-56. DOI
6. Li C, Ji Y, Wang Y, et al. Applications of metal-organic frameworks and their derivatives in electrochemical CO_2 reduction. *Nanomicro Lett* 2023;15:113. DOI PubMed PMC
7. Younus HA, Ahmad N, Ni W, et al. Molecular catalysts for CO_2 electroreduction: progress and prospects with pincer type complexes. *Coord Chem Rev* 2023;493:215318. DOI
8. Wang D, Mao J, Zhang C, et al. Modulating microenvironments to enhance CO_2 electroreduction performance. *eScience* 2023;3:100119. DOI
9. Song D, Lian Y, Wang M, et al. Electrochemical CO_2 reduction catalyzed by organic/inorganic hybrids. *eScience* 2023;3:100097. DOI
10. Fujimori S, Inoue S. Carbon monoxide in main-group chemistry. *J Am Chem Soc* 2022;144:2034-50. DOI PubMed
11. Carrilho RMB, Calvete MJF, Mikle G, Kollár L, Pereira MM. Carbon monoxide as C1 building block in fine chemical synthesis. *Chin J Chem* 2024;42:199-221. DOI
12. Wu X, Lang J, Sun Z, Jin F, Hu YH. Photocatalytic conversion of carbon monoxide: from pollutant removal to fuel production. *Appl Catal B Environ* 2021;295:120312. DOI
13. Gao D, Zhou H, Cai F, Wang J, Wang G, Bao X. Pd-containing nanostructures for electrochemical CO_2 reduction reaction. *ACS Catal* 2018;8:1510-9. DOI
14. Tan X, Yu C, Song X, et al. Robust O-Pd-Cl catalyst-electrolyte interfaces enhance CO tolerance of Pd/C catalyst for stable CO_2 electroreduction. *Nano Energy* 2022;104:107957. DOI
15. Li J, Zhang B, Dong B, Feng L. MOF-derived transition metal-based catalysts for the electrochemical reduction of CO_2 to CO: a mini review. *Chem Commun* 2023;59:3523-35. DOI
16. Bikbaeva V, Nesterenko N, García-moncada N, Valtchev V. Co-promoted Mo-carbide catalytic system for sustainable manufacturing of chemicals via co-processing of CO_2 with ethane. *Green Carbon* 2023;1:94-103. DOI
17. Li H, Gan K, Li R, et al. Highly dispersed NiO clusters induced electron delocalization of Ni-N-C catalysts for enhanced CO_2 electroreduction. *Adv Funct Mater* 2023;33:2208622. DOI
18. Mao Y, Jiang Y, Gou Q, et al. Indium-activated bismuth-based catalysts for efficient electrocatalytic synthesis of urea. *Appl Catal B*

Environ 2024;340:123189. DOI
19. Deng C, Qi C, Wu X, Jing G, Zhao H. Unveiling the relationship between structural evaluation and catalytic performance of InOOH during electroreduction of CO_2 to formate. *Green Carbon* 2024;2:124-30. DOI
20. Liang S, Huang L, Gao Y, Wang Q, Liu B. Electrochemical reduction of CO_2 to CO over transition metal/N-doped carbon catalysts: the active sites and reaction mechanism. *Adv Sci* 2021;8:e2102886. DOI PubMed PMC
21. Jia C, Ching K, Kumar PV, et al. Vitamin B_{12} on graphene for highly efficient CO_2 electroreduction. *ACS Appl Mater Interfaces* 2020;12:41288-93. DOI
22. Wang SM, Yuan X, Zhou S, et al. Single-atomic-Ni electrocatalyst derived from phthalocyanine-modified MOF for convoying CO_2 intelligent utilization. *Energy Mater* 2024;4:400032. DOI
23. Zhang Z, Yu L, Tu Y, et al. Unveiling the active site of metal-free nitrogen-doped carbon for electrocatalytic carbon dioxide reduction. *Cell Rep Phys Sci* 2020;1:100145. DOI
24. Zhang W, Jia B, Liu X, Ma T. Surface and interface chemistry in metal-free electrocatalysts for electrochemical CO_2 reduction. *SmartMat* 2022;3:5-34. DOI
25. Yadav RM, Li Z, Zhang T, et al. Amine-functionalized carbon nanodot electrocatalysts converting carbon dioxide to methane. *Adv Mater* 2022;34:e2105690. DOI
26. Dong Y, Zhang Q, Tian Z, et al. Ammonia thermal treatment toward topological defects in porous carbon for enhanced carbon dioxide electroreduction. *Adv Mater* 2020;32:e2001300. DOI
27. Li J, Zan WY, Kang H, et al. Graphitic-N highly doped graphene-like carbon: a superior metal-free catalyst for efficient reduction of CO_2. *Appl Catal B Environ* 2021;298:120510. DOI
28. Li R, Liu F, Zhang Y, Guo M, Liu D. Nitrogen, sulfur co-doped hierarchically porous carbon as a metal-free electrocatalyst for oxygen reduction and carbon dioxide reduction reaction. *ACS Appl Mater Interfaces* 2020;12:44578-87. DOI
29. Yang F, Liang C, Yu H, et al. Phosphorus-doped graphene aerogel as self-supported electrocatalyst for CO_2-to-ethanol conversion. *Adv Sci* 2022;9:e2202006. DOI PubMed PMC
30. Sreekanth N, Nazrulla MA, Vineesh TV, Sailaja K, Phani KL. Metal-free boron-doped graphene for selective electroreduction of carbon dioxide to formic acid/formate. *Chem Commun* 2015;51:16061-4. DOI PubMed
31. Zhang B, Zhang J, Zhang F, et al. Selenium-doped hierarchically porous carbon nanosheets as an efficient metal-free electrocatalyst for CO_2 reduction. *Adv Funct Mater* 2020;30:1906194. DOI
32. Sun Y, Zhao K, Deng X, Zhang M, Wang X, Wang W. Metal-free Se-based tetra-doped carbon catalyst for high-selective electro-reduction of CO_2 into CO. *J Environ Chem Eng* 2023;11:110435. DOI
33. Fu GE, Yang H, Zhao W, Samorì P, Zhang T. 2D conjugated polymer thin films for organic electronics: opportunities and challenges. *Adv Mater* 2024;29:e2311541. DOI PubMed
34. Yao L, Ma C, Sun L, et al. Highly crystalline polyimide covalent organic framework as dual-active-center cathode for high-performance lithium-ion batteries. *J Am Chem Soc* 2022;144:23534-42. DOI
35. Gu S, Hao R, Chen J, et al. A star-shaped polyimide covalent organic framework for high-voltage lithium-ion batteries. *Mater Chem Front* 2022;6:2545-50. DOI
36. Wang J, Liu H, Du C, et al. Conjugated diketone-linked polyimide cathode material for organic lithium-ion batteries. *Chem Eng J* 2022;444:136598. DOI
37. Wang Y, Liu Z, Wang C, et al. π-conjugated polyimide-based organic cathodes with extremely-long cycling life for rechargeable magnesium batteries. *Energy Stor Mater* 2020;26:494-502. DOI
38. Fang Q, Zhuang Z, Gu S, et al. Designed synthesis of large-pore crystalline polyimide covalent organic frameworks. *Nat Commun* 2014;5:4503. DOI
39. Zhang Y, Huang Z, Ruan B, et al. Design and synthesis of polyimide covalent organic frameworks. *Macromol Rapid Commun* 2020;41:e2000402. DOI
40. Han B, Ding X, Yu B, et al. Two-dimensional covalent organic frameworks with Cobalt(II)-Phthalocyanine sites for efficient electrocatalytic carbon dioxide reduction. *J Am Chem Soc* 2021;143:7104-13. DOI
41. Han B, Jin Y, Chen B, et al. Maximizing electroactive sites in a three-dimensional covalent organic framework for significantly improved carbon dioxide reduction electrocatalysis. *Angew Chem Int Ed* 2022;61:e202114244. DOI
42. Feng DM, Zhu YP, Chen P, Ma TY. Recent advances in transition-metal-mediated electrocatalytic CO_2 reduction: from homogeneous to heterogeneous systems. *Catalysts* 2017;7:373. DOI
43. Feng D, Zhou L, White TJ, Cheetham AK, Ma T, Wei F. Nanoengineering metal-organic frameworks and derivatives for electrosynthesis of ammonia. *Nanomicro Lett* 2023;15:203. DOI PubMed PMC
44. Duan H, Li K, Xie M, et al. Scalable synthesis of ultrathin polyimide covalent organic framework nanosheets for high-performance lithium-sulfur batteries. *J Am Chem Soc* 2021;143:19446-53. DOI
45. Hiragond C, Kim H, Lee J, Sorcar S, Erkey C, In S. Electrochemical CO_2 reduction to CO catalyzed by 2D nanostructures. *Catalysts* 2020;10:98. DOI
46. Wang T, Xue R, Chen H, et al. Preparation of two new polyimide bond linked porous covalent organic frameworks and their fluorescence sensing application for sensitive and selective determination of Fe^{3+}. *New J Chem* 2017;41:14272-8. DOI
47. Han Y, Zhang M, Zhang YQ, Zhang ZH. Copper immobilized at a covalent organic framework: an efficient and recyclable heterogeneous catalyst for the Chan-Lam coupling reaction of aryl boronic acids and amines. *Green Chem* 2018;20:4891-900. DOI

48. Liebl MR, Senker J. Microporous functionalized triazine-based polyimides with high CO_2 capture capacity. *Chem Mater* 2013;25:970-80. DOI
49. Jerkiewicz G. Applicability of platinum as a counter-electrode material in electrocatalysis research. *ACS Catal* 2022;12:2661-70. DOI